The role of cross-field transport in a benchmark of DIV1D, a new dynamic 1D divertor model, on the 2D SOLPS-ITER code

G L Derks[1,2,3]**, J P K W Frankemölle**[1,3]**, J T W Koenders**[1,2]**, M van Berkel**[1]**, H Reimerdes**[4]**, M Wensing**[4]**, E Westerhof**[1]

[1] DIFFER - Dutch Institute for Fundamental Energy Research, De Zaale 20, 5612 AJ Eindhoven, the Netherlands

[2]Eindhoven University of Technology, Control Systems Technology, Eindhoven, The Netherlands

[3] Eindhoven University of Technology, Science and Technology of Nuclear Fusion, Eindhoven, The Netherlands

[4] Ecole Polytechnique Fédérale de Lausanne (EPFL), Swiss Plasma Center (SPC), Lausanne, Switzerland

E-mail: `g.l.derks@differ.nl`

June 2022

Abstract. In this paper we present DIV1D, a new 1D dynamic physics-based model of the divertor plasma under development to study and control the dynamics of detached plasmas. We developed a novel 1D mapping of static 2D SOLPS-ITER divertor plasmas to demonstrate that DIV1D can self-consistently match 2D SOLPS-ITER static solutions and dynamically transition between these solutions. The self-consistent description in DIV1D is ascribed to the unique account of cross-field transport with an effective flux expansion and a neutral gas background. The benchmark serves as a basis to validate dynamics in DIV1D in order to guide control efforts.

Keywords: dynamic, detachment, simulation

1. Introduction

Fusion reactors require real-time feedback control to handle the enormous heat and particle fluxes that come from the ignited core plasma. These fluxes are exhausted on the wall in the heat exhaust called the divertor [1]. To reduce heat loads to the divertor targets and stay within material limits, heat exhaust controllers should bring and maintain the divertor plasma in a (marginally) detached regime characterized by low plasma temperature and pressure. Although detached plasmas are simulated with increasing accuracy by large-scale physics-based models, excessive computation times for dynamic cases necessitate fast complimentary reduced dynamic models for the design, verification and validation of heat exhaust controllers for future reactors.

In this paper we present DIV1D [2], a new 1D dynamic physics-based model of the divertor plasma that is specifically being developed to study the dynamics of detached plasmas. We benchmark DIV1D on 2D SOLPS-ITER simulations that scan gas puff magnitudes and are based on a TCV plasma equilibrium. The goal of this benchmark is to test if DIV1D can self-consistently match 2D SOLPS-ITER static solutions of TCV plasmas and dynamically transition between these solutions. We present a novel 1D mapping of static 2D SOLPS-ITER divertor plasmas that captures the heat as it flows from a region below the X-point (upstream) to the target plates. The 1D mapped SOLPS-ITER profiles are compared with DIV1D profiles to gain insights from discrepancies and regions of correspondence.

The benchmark serves as a basis to further investigate dynamics of the scrape-off layer with DIV1D. Eventually DIV1D is not meant to replace large code suites, but for a complementary role in fast dynamic investigations. Instances are investigations into ELM buffering [3] and the physics behind the dynamics as observed in various system identification experiments [1, 4, 5]. Such investigation might eventually provide a physics basis to generate reduced dynamic models (i.e. transfer functions in [5]) to guide tokamak heat exhaust control efforts.

The remainder of the paper is structured as follows. We start detailing DIV1D, a dynamic 1D code for the scrape-off layer and then explain how this can be compared to 2D solutions of SOLPS-ITER. Profiles of DIV1D and SOLPS-ITER are compared in section 4 and the role of cross-field transport is evaluated in section 5. Finally results are discussed.

2. DIV1D: a 1D numerical code for divertor plasma simulation

We start from the assumption that the behavior of the divertor plasma is dominated by the 1D dynamics along the magnetic field lines. In addition the plasma is assumed to be quasi-neutral and the ion and electron fluids are assumed to be strongly coupled resulting in equal ion and electron temperatures. This then results in a set of balance equations for the plasma density, momentum, and energy as well as for the neutral density, which is very similar to the set of equations as implemented by various authors in their respective 1D codes [6–9]. A schematic of DIV1D is depicted in figure 1 for which the following sections details the equations, sources, sinks, and boundary conditions.

2.1. Equations

The equations solved are: the particle balance equation, the plasma momentum balance, the plasma energy balance, and an equation for the evolution of the neutral particle density. As in Nakazawa et al. [6], neutral momentum and energy are ignored.

The plasma particle balance is given by

$$\frac{\partial n}{\partial t} = -B\frac{\partial}{\partial x}\left(\frac{\Gamma_n}{B}\right) + S_n, \tag{1}$$

where n is the plasma (electron) density, $\Gamma_n = nv_\parallel$ is the convective particle flux (a possible effect of diffusion is ignored) with $v_\parallel$ the parallel velocity, and S_n represent the sum of all particle sources and sinks. B represents the magnitude of the total magnetic field. The magnetic field is assumed to have a radial dependence ($B \propto 1/R$) and is described by the flux expansion parameter ε_f as

$$B = \left[1 + (\varepsilon_\mathrm{f} - 1)x/L\right]^{-1} \tag{2}$$

with the domain length L discretized into cells with positions in coordinate x. Here and in the equations below, the inclusion of B accounts for the effect of flux expansion due to a varying total magnetic field [7, 8].

The momentum balance is given for the ions by

$$\frac{\partial nmv_\parallel}{\partial t} = -B\frac{\partial}{\partial x}\left(\frac{nmv_\parallel^2}{B}\right) - \frac{\partial}{\partial x}p + S_\mathrm{mom}, \tag{3}$$

where m is the mass of the dominant ion species (default Deuterium $m = 3.3436 \times 10^{-27}$ kg) , $p = 2neT$ is the total plasma pressure (we will use T in units eV such that the Boltzmann constant can be equated with the elementary charge e to obtain the pressure in Pascal), and S_mom represents the sum of all momentum sources and sinks.

Ion and electron temperatures are considered equal such that only one energy balance needs to be solved. The internal energy ($3nkT$) balance of the plasma is then given by

$$\frac{\partial 3neT}{\partial t} = -B\frac{\partial}{\partial x}\left(\frac{q_\parallel}{B}\right) + v_\parallel\frac{\partial}{\partial x}p + S_\mathrm{ene}, \tag{4}$$

where the heat flux $q_\parallel$ is given by the equation

$$q_\parallel = 5neTv_\parallel - \kappa_\parallel\frac{\partial}{\partial x}T, \tag{5}$$

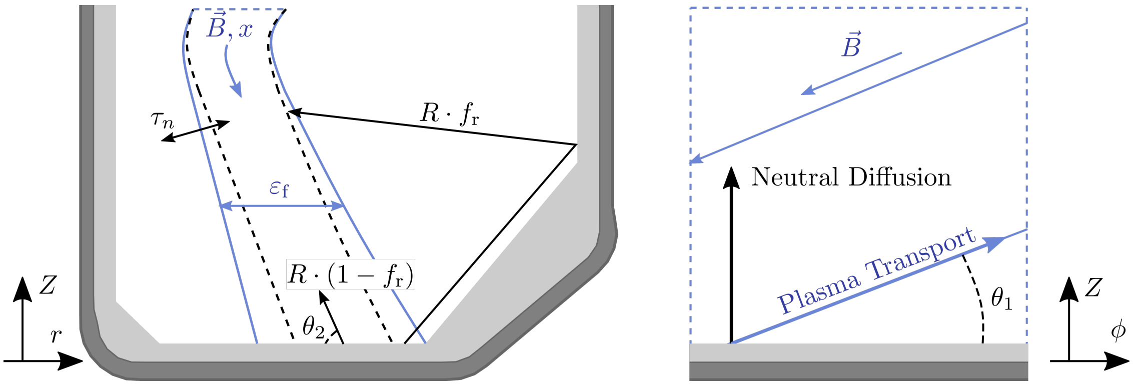

Figure 1. Schematic of DIV1D. (left) A poloidal schematic of the DIV1D grid that is defined along the x coordinate aligned with the magnetic field $\vec{B}$ (T) and considering the effect of flux expansion ε_f. At the wall, ions recycle into neutrals that remain in the plasma $R \cdot (1 - f_\mathrm{r})$ or are redistributed $R \cdot f_\mathrm{r}$. Neutrals are lost or exchanged with the neutral gas background volume on timescale τ_n (s). (right) Schematic along the toroidal direction ϕ depicting neutral diffusion perpendicular to the wall and plasma transport along magnetic field lines.

where the first term on the right hand side represents the total enthalpy flux and the second term represents the parallel heat conduction with (for T in eV) the parallel conductivity being given by $\kappa_\parallel = 2 \times 10^3 T^{5/2}$ J/eVms (see Chapter 4.10.1 of [10]). S_ene represent the sum of all internal energy sources and sinks.

The neutral particle balance is given by

$$\frac{\partial n_\mathrm{n}}{\partial t} = \frac{\partial}{\partial x} D \frac{\partial}{\partial x} n_\mathrm{n} + S_\mathrm{neutral}, \tag{6}$$

where n_n is the neutral particle density and D is the neutral particle diffusion coefficient which is given by [6]

$$D = \frac{eT}{m\nu_\mathrm{cx} \sin^2\theta}, \tag{7}$$

where θ is the angle at which the magnetic field hits the target, and $\nu_\mathrm{cx} = n\langle\sigma_\mathrm{cx} v\rangle$ is the charge exchange collision frequency for the neutrals and the average charge exchange rate $\langle\sigma_\mathrm{cx} v\rangle$ is specified below. The factor $\sin^2\theta$ appears in the equation for the neutral diffusion because the neutrals are free to move across magnetic field lines, such that their motion perpendicular to the target surface results in an effective parallel displacement that is increased by a factor $1/\sin\theta$. The angle θ is a function of the magnetic field $(B_\mathrm{tot}/B_\theta)$ and represented by a combination of θ_1 and θ_2 in figure 1.

The neutral momentum and energy balances are ignored such that all momentum and energy that goes to neutrals in collisions is lost. In TCV, the mean free path of neutrals outside the SOL easily exceeds the vessel size [11]. Consequently, neutrals that leave the SOL quickly distribute their energy and momentum to the surroundings. For the high neutral pressures in ITER the mean free path for neutrals is a few orders of magnitudes smaller (around a centimeter or millimeter) such that the neutrals in the SOL are likely more conservative on momentum and energy. For ITER divertor plasmas it might thus be worthwhile to extend the neutral description of DIV1D while neglecting neutral momentum and energy seems to represent the physics at play for TCV plasmas.

2.2. Boundary Conditions

Each of the equations requires boundary conditions at the upstream point $x = 0$ and at the target $x = L$, where L is the given length of the flux tube. Upstream we use the following boundary conditions: the plasma density at the upstream point is given: $n(x = 0) = n_\mathrm{e,u}$; the upstream plasma momentum flux is assumed to be constant: the upstream parallel heat flux is given: $q_\parallel(x = 0) = q_{\parallel,\mathrm{u}}$; and finally, the upstream neutral particle density is assumed to have zero gradient.

The boundary conditions at the target are given by the usual sheath boundary conditions (see Section 2.8 in [10]) assuming that density and temperature are constant across the sheath, while the plasma particle flux and momentum are given by the Bohm condition, $\Gamma_n(x = L) \geq nc_\mathrm{s}$ and where $c_\mathrm{s} = \sqrt{2eT/m}$ is the plasma sound speed, and the heat flux on the target is given by the sheath heat transmission factor γ which can be specified as input ($\gamma = 6$ for the DIV1D simulations in this contribution):

$$q_\parallel(x = L) = \gamma neTc_\mathrm{s}. \tag{8}$$

The neutral particle flux coming from the target is determined by the recycling coefficient R and a redistribution fraction f_r given on input, i.e. $\Gamma_\mathrm{neutral}(x = L) = -R(1 - f_r)\Gamma_n(x = L)$. Note that when $R = 1$ the total number of particles should be conserved requiring a zero upstream plasma inflow velocity in case of a steady state solution. The redistribution fraction projects a fraction of the recycling flux as a homogeneous neutral source along the divertor leg and is further detailed in the end of the following section on sources and sinks.

2.3. Sources and Sinks

The various sources and sinks are determined mostly by atomic processes like charge exchange, ionization, excitation, and recombination.

For the plasma density the sources and sinks are given by ionization and recombination respectively:

$$S_n = +nn_n\langle\sigma_{\mathrm{ion}}v\rangle - n^2\langle\sigma_{\mathrm{rec}}v\rangle. \tag{9}$$

Because the neutral particle momentum is neglected there is no momentum source, while the momentum sinks are induced by charge exchange and recombination

$$S_{\mathrm{mom}} = -nmv_{\parallel}\left(n_n\langle\sigma_{\mathrm{cx}}v\rangle + n\langle\sigma_{\mathrm{rec}}v\rangle\right). \tag{10}$$

The energy balance contains both heat sinks and sources associated with charge exchange, hydrogenic ionization, and excitation, radiative and three-body recombination as well as impurity radiation

$$\begin{aligned} S_{\mathrm{ene}} = & -1.5neT\left(n_{\mathrm{n}}\langle\sigma_{\mathrm{cx}}v\rangle + 2n\langle\sigma_{\mathrm{rec}}v\rangle\right) && (11a)\\ & + \frac{1}{2}nmv_{\parallel}^2 n_n\langle\sigma_{\mathrm{ion}}v\rangle && (11b)\\ & - nn_{\mathrm{n}}\langle E_{\mathrm{ion}}\sigma_{\mathrm{ion}}v\rangle - nn_{\mathrm{n}}\langle E_{\mathrm{exc}}\sigma_{\mathrm{exc}}v\rangle && (11c)\\ & + n^2\left\langle E_{\mathrm{el}}\sigma_{\mathrm{rec}}v\right\rangle - n^2\left\langle E_{\mathrm{rad}}\sigma_{\mathrm{rec}}v\right\rangle && (11d)\\ & - n^2\xi_{\mathrm{Z}}L_{\mathrm{Z}}(T) && (11e) \end{aligned}$$

where the first line (i.e. equation 11*a*) represents the losses to the neutrals due to charge exchange and recombination and the second line is a source term from friction with the neutrals that comes from ionization of (assumed momentum less) neutrals. The third line comes from ionization and the associated excitation, where $E_{\mathrm{ion}} = 13.6$ eV is the ionization energy and E_{exc} is the energy loss per excitation. In practice these are typically combined into an effective energy loss per ionization (see Appendix A for the implemented reaction rates). The fourth line represents the effective energy balance from three-body and radiative recombination. Finally, in the last line, $L_{\mathrm{Z}}(T)$ is the radiative cooling rate of the impurity with concentration ξ_{Z} for the specified impurity Z.

What is a sink for the plasma density is a source for the neutral particles, while additional neutral particle sources are associated with gas puff, redistribution of recycled neutrals or a possible exchange with a neutral gas background, such that

$$S_{\mathrm{neutral}} = -S_n + S_{\mathrm{puff}} - \frac{n_{\mathrm{n}} - n_{\mathrm{b}}}{\tau_{\mathrm{n}}} + \frac{n(L)v_{\parallel}(L)Rf_{\mathrm{r}}}{L} \tag{12}$$

where S_{puff} is a neutral particle source from an additional gas puff, τ_{n} accounts for a finite residence time of the neutral particles [8, 9], and a fraction f_{r} of the recycling flux can be redistributed homogeneously over the entire leg. Unique in DIV1D is the possibility to specify a finite background neutral gas density n_{b} such that the residence time τ_{n} becomes an exchange time for neutrals in the leg with neutrals in the background gas. Consequently, the exchange time for the neutrals accounts for cross-field neutral particle transport across the scrape-off layer and perpendicular to the flux tube (i.e. to the parallel transport correction with the pitch angle θ). In case of nonzero n_{b}, the terms τ_{n} and f_{r} aim to model similar physics of redistributing neutrals and f_{r} should be equated to zero, while the recycling coefficient R should be reduced to include only the recycled neutral particle remaining inside the effective plasma flux tube. The atomic rates for charge exchange, recombination, ionization, and excitation as used in DIV1D are presented in Appendix A next to a radiative cooling function for Carbon. An overview of input parameters is provided Appendix B.

3. A novel method to benchmark 1D divertor models on 2D divertor solutions

This section presents one of the key contributions of this work: the adoption of a method to map 2D equilibria of SOLPS-ITER into 1D profiles along the divertor leg for comparison and benchmarking of 1D divertor models. The simulation settings and 2D outputs SOLPS-ITER are briefly discussed and followed by the mapped 1D profiles that form the basis to benchmark DIV1D as a self-consistent divertor model.

3.1. SOLPS-ITER settings and its 2D outputs

The SOLPS-ITER code [12] is a combination of the 2D multi-fluid plasma transport code B2.5 and the 3D kinetic Monte Carlo neutral transport code EIRENE. The following paragraphs evaluate the settings of the SOLPS-ITER simulations used in this work and familiarize the reader with its 2D outputs.

The SOLPS-ITER simulations used in this contribution represent a gas puff scan and are based on TCV discharge #62807. This was a reversed field heated L-mode discharge with only Ohmic heating where a plasma current of 250 kA heated the core plasma with a power of 360 kW. Core densities and temperatures reach 10^{20} m^{-3} and 500 eV respectively. The assumptions and settings used in SOLPS-ITER are similar to those in [13] and account for electric currents, drifts and kinetic neutrals. The radial transport coefficients are set spatially constant and species α independent as $D_{\perp,\alpha} = 0.2$ m^{2}s^{-1} for particle diffusion and $\chi_{\perp,\alpha} = 1$ m^{2}s^{-1} for heat conduction. The sheath heat transmission coefficient is found to be approximately $\gamma \approx \gamma_{\mathrm{e}} + \gamma_{\mathrm{i}} = 1.5 + 1.5 + e\phi/T_e \approx 5.7$, where the sheath heat transmission coefficient of ions is set to $\gamma_{\mathrm{i}} = 1.5$ and the secondary heat transmission coefficient of electrons is set to $\gamma_e^{2nd} = 0.5$ while the contribution due to the potential drop from the magnetic presheath entrance towards the targets is accounted for using the value of the electrostatic potential ϕ in the respective cell adjacent to the target surface (see page 79 in [14]). Carbon impurities are introduced through physical sputtering using the Roth-Bogdansky formula and a constant chemical sputtering yield of 3.5%. A source of deuterium molecules at the valve location emulates a constant gas puff while a species-independent recycling coefficient $R = 0.99$ emulates particle pumping.

To familiarize the reader with 2D SOLPS solutions, figure 2 presents the parallel heat flux $q_\parallel$ from SOLPS simulation 150683 on the B2.5 grid. The B2.5 grid coincides with the magnetic topology such that the y direction is aligned with the magnetic field and the x direction is perpendicular to the magnetic field. Solutions on the B2.5 grid cover the edge-core and scrape-off layer plasma. In the remainder of this paper plasma *profiles* are a function of the y-direction and aligned with the magnetic field whereas plasma *distributions* are a function of the x-direction and go across the leg.

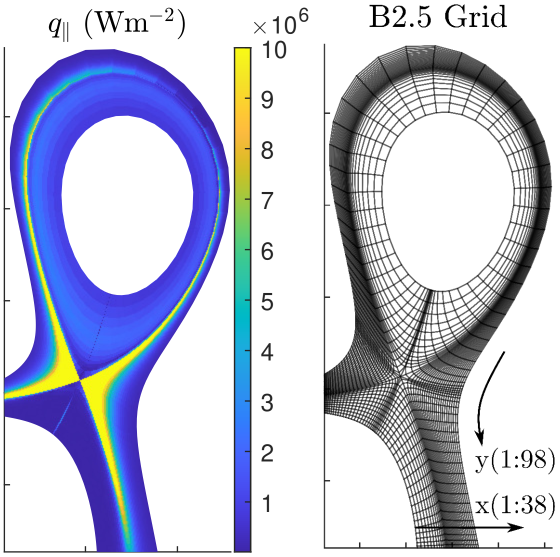

Figure 2. Overview of the parallel heat flux (left) plotted on the B2.5 grid (right) from SOLPS-ITER simulation 150683. The y direction of the B2.5 grid is aligned with the magnetic field. The x and y directions are split into 38 and 98 cells respectively.

3.2. Mapping SOLPS-ITER solutions to 1D

In [7], 1D solutions were extracted from 2D SOLPS-ITER equilibria by considering single flux tubes to benchmark SOLF1D, a model that is similar to DIV1D. The single flux tube represents a convenient 1D solution of SOLPS-ITER because the grid is aligned with the magnetic field (i.e. the y-direction in figure 2). However, the plasma profiles in single flux tubes of SOLPS-ITER depend to a great extend on cross-field transport. Consequently, the single flux tube has two limitations in a benchmark of DIV1D as a 1D model for the divertor plasma.

Firstly, cross-field transport terms with adjacent flux tubes must be approximately modeled when DIV1D is compared to a single flux tube of the 2D SOLPS-ITER equilibria. In their benchmark, [7] modeled cross-field transport by extracting particle, momentum, and energy sources directly from 2D SOLPS-ITER equilibria. Imposing these sources as boundary conditions for their 1D SOL code called SOLF1D, [7] found agreement within single percentages to single flux tubes from 2D equilibria. Although impressive, this is not a suitable approach for DIV1D as it should self-consistently model the divertor and therefore cannot rely on 2D equilibria to provide detailed sources and sinks.

Secondly, single flux tubes do not reflect macroscopic plasma behavior in the divertor. Figure 3 details the heat flux as it flows from the X-point to the wall. The left shows that the full width at half the max (FWHM) of the heat flux (in red) is centered around tube 15 near the X-point and that it drifts outwards to tube 25 at the target. Due to the outward drift, the parallel heat flux distributions on the right show that tube 15 slightly underestimates the target heat flux while tube 25 clearly underestimates the upstream heat flux. When the heat flux drifts across flux tubes it is thus evident that a single flux tube in the B2.5 grid cannot represent macroscopic plasma behavior in the divertor.

The two above limitations are resolved in this work by considering a FWHM heat flux channel in order to map 2D SOLPS-ITER equilibria to 1D profiles. Following the experimental methodology in [15], the FWHM heat flux channel is bounded by the full width of the heat flux distributions at half the maximum values. The cells that roughly cover the full width at half the maximum (FWHM) of the heat flux are selected from the B2.5 grid (see left red area in figure 3). The area covered by these cells is found to contain approximately 70% of the heat flux that is flowing from X-point to the target. Quantities are averaged on the covered area to obtain 1D profiles along the leg while minimum and maximum values provide a distribution interval. The mapped 1D profiles as extracted from 2D SOLPS-ITER simulation 150683 are presented in figure 4. It can be seen that the minimum values of shaded area for the heat flux q are not exactly half the maximum values, this is because the cells only roughly cover the full width at half the maximum and interpolation was avoided. The FWHM heat flux channel resolves the limitations encountered in a benchmark of DIV1D with a single flux tube as follows.

Firstly, cross-field plasma transport now results in

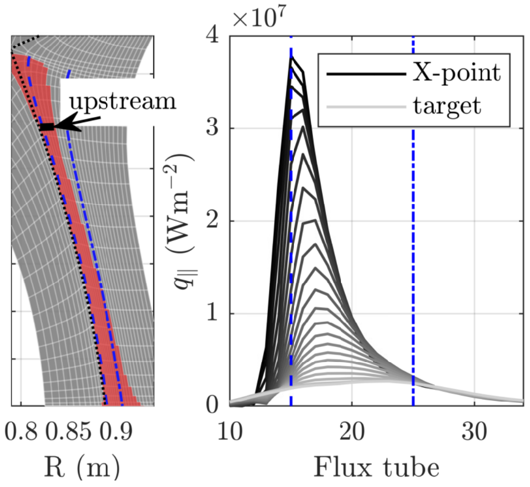

Figure 3. (left) Poloidal overview of the region where the full width at half the maximum of the heat flux flows in red and two flux tubes in blue. Above the cutoff the 2D equilibria are not mapped to 1D for comparisons, this thus denotes the upstream point. (right) Radial distributions as function of flux tube for the heat flux. Profiles change color from X-point in black (y=74) to the target in lightest gray (y=98). The two blue flux tubes are located at the peak upstream heat flux (15) and peak target heat flux (25). Flux tube 15 underestimates the target heat flux by a factor 2 while flux tube 25 underestimates the upstream peak heat flux by a factor 5.

a changing geometry of the FWHM heat flux channel. Cross-field plasma transport causes the profile to widen and the effective cross-sectional tube area to increase. There are thus no cross-field plasma sources on the boundaries of the FWHM channel and these do not have to be modeled based on detailed 2D equilibria. Instead, DIV1D can make use of the flux expansion factor ε_f to mimic the expansion of the FWHM heat flux channel due to cross-field transport.

Secondly, the FWHM mapping of 2D SOLPS-ITER equilibria provides information about the validity of a 1D description for the divertor plasma. In a 1D description, the plasma distributions across the leg are approximated by scalar values. The intervals around the profiles (i.e. patches in figure 4) provide the range of plasma values that are lumped into scalar quantities. Near the X-point, the intervals indicate an increased variation in values, that is likely due to 2D effects. To avoid 2D effects and to provide well-defined upstream conditions for DIV1D, the upstream point is selected at five meters from the target. The upstream point is indicated in black in figures 2 and 4. Since large variations due to 2D effects are avoided, the mapped 1D profiles below five meters are considered as a physical 1D description of the divertor plasma.

To summarize, we presented a method to map 2D SOLPS-ITER equilibria into 1D profiles along the divertor leg. The mapping averages over the FWHM area of the heat flux to obtain 1D profiles while variations in values across the area provide a measure of the validity of a 1D description. In the following section, the FWHM mapped 1D profiles of 2D SOLPS-ITER equilibria are used to benchmark DIV1D as a code to self-consistently describe the divertor plasma.

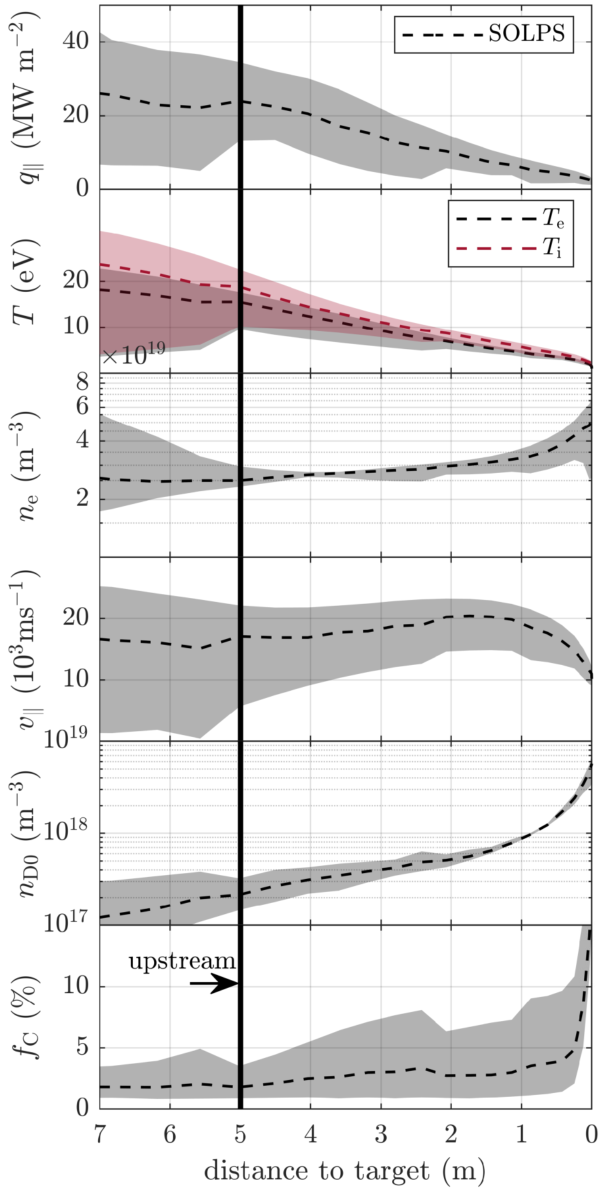

Figure 4. Overview of 2D SOLPS-ITER solutions mapped to 1D profiles below the X-point for parallel heat flux $q_\parallel$, electron and ion temperatures $T_\mathrm{e,i}$, electron density n_e, parallel velocity $v_\parallel$, neutral density n_D0 and carbon fraction f_C. The shaded areas represent minimum and maximum values of quantities in the channel covering the FWHM of the heat flux distributions along the leg.

4. Benchmark of DIV1D on 1D mapped SOLPS-ITER solutions

To benchmark DIV1D, a set of eight SOLPS-ITER simulations was selected that represents a gas puff scan for a TCV L-mode plasma. The goal of the benchmark is to test if DIV1D can self-consistently describe the relation between upstream (near X-point) and target plasma conditions.

4.1. Settings for DIV1D simulations

The settings for SOLPS-ITER were discussed in section 3.1. The settings for DIV1D are chosen to match the mapped 1D SOLPS profiles as follows: connection length $L = 5$ m, upstream heat flux $q_{\|,\mathrm{u}} = 22$ MWm^{-2}, carbon fraction $f_\mathrm{C} = 3\%$, incident angle $\sin(\theta) = 0.06$ and *effective* flux expansion factor $\varepsilon_\mathrm{f} = 2.3$. These quantities are nearly constant across the 1D mapped SOLPS-ITER simulations under consideration (see Appendix C for details). The recycling coefficient R is set to 99%, equal to SOLPS-ITER. The redistribution factor f_r is not used and set to zero. The neutral exchange time is chosen as $\tau_\mathrm{n} = 3$ μs. This choice is in-line with and constrained by the exchange distance $d \approx 0.01 - 0.1$m (i.e. width of the divertor leg) divided by an approximate thermal neutral velocity $v \approx 1 - 3 \cdot 10^4$ ms^{-1} (i.e. kinetic energies of 1 to 10 eV). The upstream density $n_{\mathrm{e,u}}$ and neutral gas background density n_b are not constant but varied as function of 1D mapped SOLPS-ITER simulations, their functional dependence is depicted in figure 5. The two SOLPS-ITER simulations in the blue box of figure 5 are excluded from the comparison because the ion and electron temperatures are discrepant and not in-line with the assumption of equal temperatures in DIV1D. Simulations of DIV1D were checked for code errors with two-point formatting following [16] (see Appendix D). The following section will elaborate on the comparison of DIV1D with SOLPS-ITER.

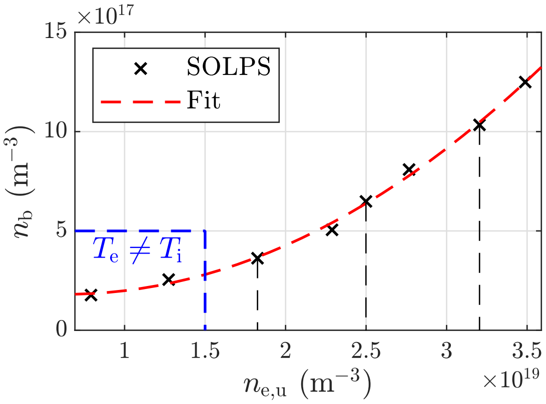

Figure 5. The functional dependence between the background neutral gas density and upstream plasma density extracted from mapped 1D SOLPS-ITER profiles. The black dashed lines mark the SOLPS profiles that are compared to DIV1D profiles. Simulations in the blue dashed box are excluded because ions and electrons are weakly coupled, i.e. $T_\mathrm{e} \neq T_\mathrm{i}$. See Appendix C for details. Fit: $y = [2.3 - 1.6x10^{-19} + (1.3x10^{-19})^2]10^{17}$.

4.2. Comparing profiles of DIV1D and 1D mapped SOLPS-ITER for varying upstream densities

This subsection compares profiles of DIV1D to the 1D mapped SOLPS-ITER simulations. This comparison will evaluate whether DIV1D produces shapes that are similar to mapped SOLPS-ITER solutions across the range of considered SOLPS-ITER simulations.

A simulation of DIV1D with good correspondence to 1D mapped SOLPS-ITER profiles is depicted in figure 6. The simulation has an upstream electron density of $2.5 \cdot 10^{19}$ m^{-3} and corresponds to the second dashed black vertical line in figure 5. From the profiles in figure 6 it can be seen that the profiles of DIV1D for the parallel heat flux $q_\|$, electron density n_e, and neutral density n_{D0} are close to the averaged SOLPS-ITER profiles and within the shaded areas. The temperature profile of DIV1D is very similar to SOLPS-ITER but a few eV higher around a distance of two to three meters to the target. The velocity profile of DIV1D is higher than for SOLPS-ITER. Following analysis in [17], we compared with SOLPS-ITER simulation 150684 without drifts and found that the discrepancy reduces as the radial electric field no longer exerts a force on the ions towards the X-point. The remaining discrepancy might be due to the particle balance in DIV1D and indicates that more ions are lost in the divertor compared to SOLPS. These observations and discrepancies are similar across simulations with upstream densities in the range of $n_{\mathrm{e,u}} = 1.8 - 2.8 \cdot 10^{19}$ m^{-3}.

The profiles of the DIV1D simulation with the lowest upstream density in the comparison is depicted in figure 7. The simulation has an upstream electron density of $1.8 \cdot 10^{19}$ m^{-3} and corresponds to the first dashed black vertical line in figure 5. It can be seen that the electron density n_e of DIV1D flattened and that the upstream ion velocity $v_\|$ increased compared to results in figure 6. Simulations of DIV1D with lower densities are not considered because the ion and electron temperatures decouple in SOLPS-ITER simulations. In addition, the heat flux in SOLPS-ITER becomes limited by the flow of electrons as there are too little collisions to conduct the heat. To correctly model this, DIV1D should likely have flux limiters (see page 66 in [14]) and separately consider temperatures of ions and electrons, features which are currently not in place.

At high densities, the correspondence between profiles of DIV1D and 1D mapped SOLPS-ITER starts to deteriorate. In figure 8 we consider the simulation

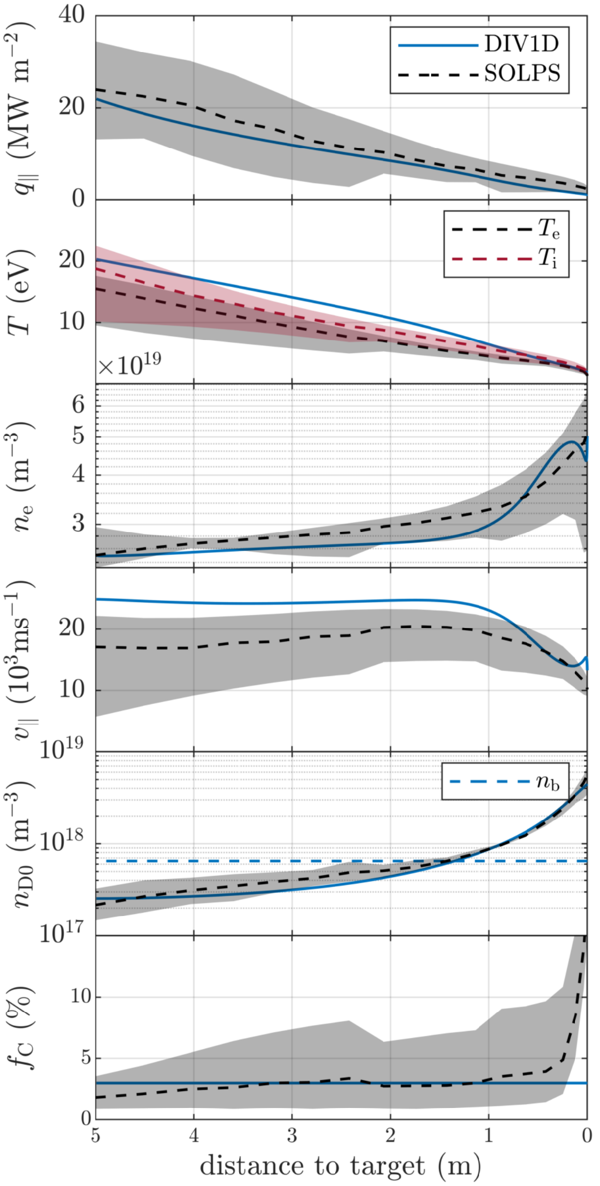

Figure 6. Comparison of DIV1D with 1D mapped SOLPS-ITER profiles of simulation 150683 (second dashed line in figure 5). On display are the profiles for parallel heat flux, temperature, electron density, ion velocity, and neutral density in scrape-off layer and gas background. The profiles of DIV1D lie almost within the intervals of the 1D mapped profiles except for the temperature and velocity, where the solution of DIV1D is above that of 1D mapped profiles.

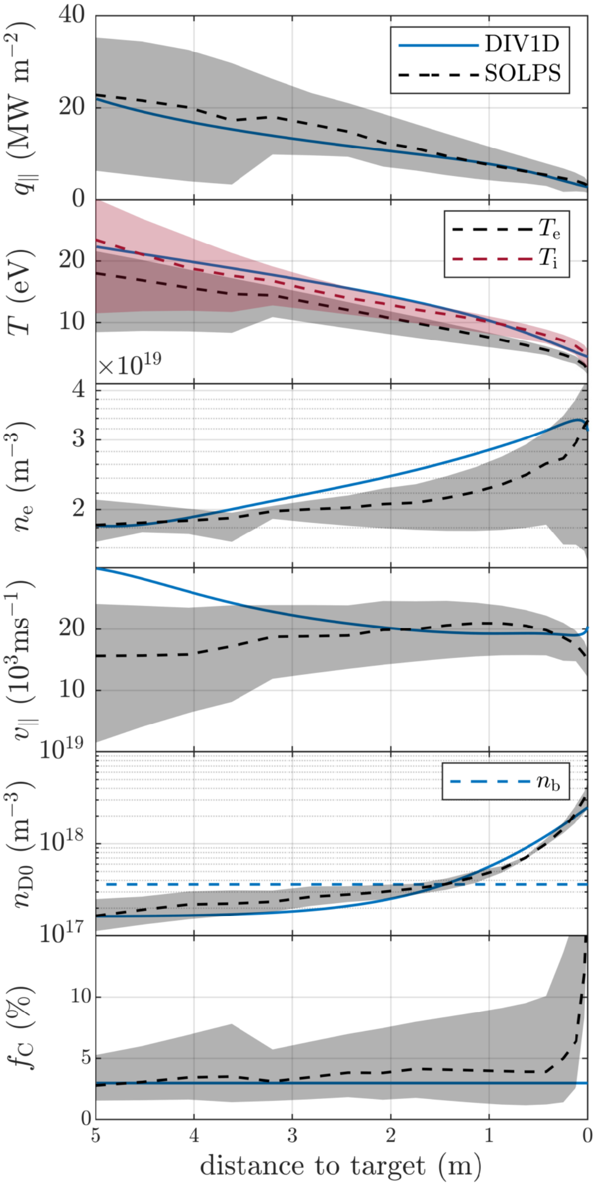

Figure 7. Comparison of DIV1D with 1D mapped SOLPS-ITER profiles of simulation 150678 (first dashed line in figure 5). The profiles are very similar, but the upstream ion velocity of DIV1D is ten km/s higher than that of SOLPS-ITER.

with a density of $n_{e,u} = 3.2 \cdot 10^{19}$ m^{-3}. A small discrepancy formed for the heat flux of DIV1D in front of the target which dropped slightly below that of SOLPS-ITER. Additionally, the upstream temperature of DIV1D rises one to five eV above SOLPS-ITER. SOLPS-ITER accounts for carbon transport in space and across ionization stages and considers energy losses on a distribution across the leg. These effects likely distribute energy losses more evenly along the leg [18, 19], and reduce the sharper transition in temperature DIV1D has around two meters to the target. Larger differences are observed for the density n_e and the velocity $v_\parallel$.

The density n_e of DIV1D first drops below SOLPS-ITER around 3.5 meters to the target and rises above SOLPS-ITER from 1.5 meters to the target. For the velocity $v_\parallel$ the inverse can be observed as it is first higher and then drops below values from SOLPS-ITER. The difference in shapes for the electron density and velocity might be a result from friction forces between flux tubes that level the velocity profile which in turn levels the density profile. These are not accounted for by DIV1D as it simulates a single tube. Alternative explanations include transport affected reaction rates for atomic processes, a flux expansion profile that is different from the relation in equation 2, or a discrepancy in the exchange of neutrals with the background. These are subjects for further investigations. The following sections will compare solutions as function of upstream density.

4.3. Comparing scalar quantities of DIV1D and 1D mapped SOLPS-ITER for varying upstream densities

The solutions of the divertor plasma evolve as function of the upstream density. This section will compare the solutions of DIV1D and 1D mapped SOLPS-ITER on: target and upstream temperature; target density; target ion flux; power loss fraction f_{pwr}; and the momentum loss fraction f_{mom}.

The target ion flux is visible in figure 9, where it can be seen that the target flux of DIV1D lies within the interval of the 1D mapped SOLPS-ITER profiles. This means that, like SOLPS-ITER, DIV1D does not produce a roll-over with upstream density that was observed in experiments [13]. As pointed out in [8,20,21], the roll-over discrepancy could be related to molecular contributions or momentum losses.

Figure 10 depicts upstream temperatures and shows that temperatures of DIV1D lie within the ion temperature interval of SOLPS-ITER for $n_{\mathrm{e,u}} < 3 \cdot 10^{19}$ m^{-3}. However there is a weaker trend resulting in a rough five eV discrepancy at the highest density of $n_{\mathrm{e,u}} = 3.5 \cdot 10^{19}$ m^{-3}. At low densities ($n_{\mathrm{e,u}} < 1.5 \cdot 10^{19}$ m^{-3}) the ion and electron temperatures of SOLPS-ITER diverge, reaching differences from ten to twenty eV for the averaged values while shaded areas separate.

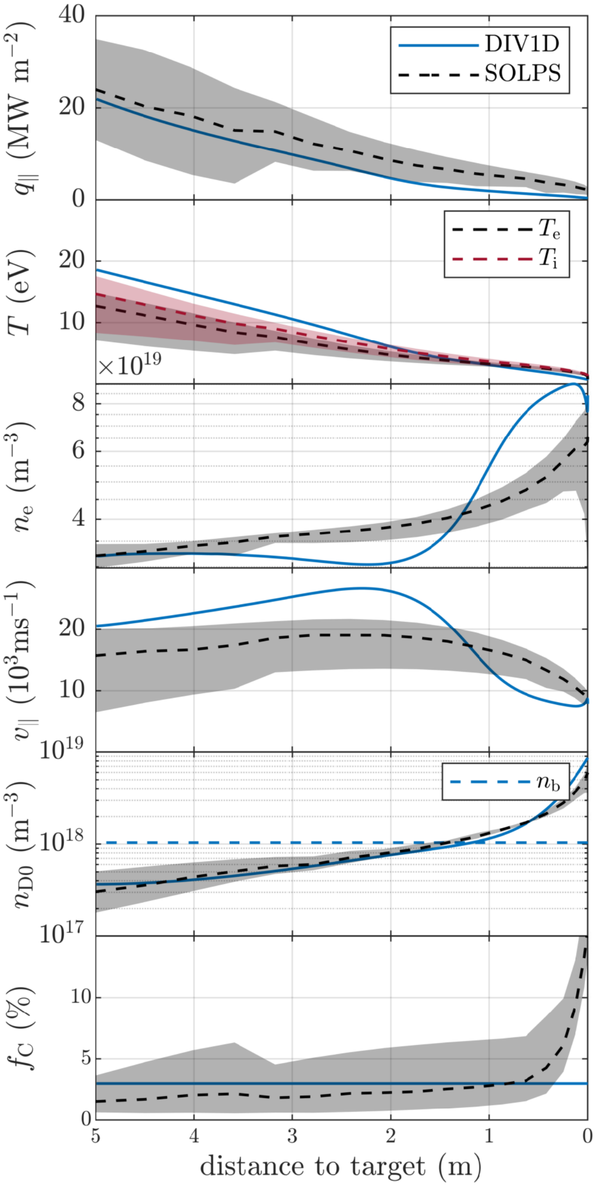

Figure 8. Comparison of DIV1D with 1D mapped SOLPS-ITER profiles of simulation 150688 (third dashed line in figure 5). On display are the profiles for parallel heat flux, temperature, electron density, ion velocity, and neutral density in scrape-off layer and gas background. The notable discrepancies for DIV1D are: a higher temperature upstream and different shapes in velocity and density profiles.

The target temperature is visible in figure 11 and shows that DIV1D follows the trend in ion temperature of SOLPS-ITER for $n_{\mathrm{e,u}} = 1.8 - 2.8 \cdot 10^{19}$ m^{-3} and drops below at higher upstream densities. This discrepancy is possibly caused by neglecting the neutral energy and momentum balances resulting in the loss of Franck-Codon recycling energy and residual neutral energy in of charge-exchanged ions. At low densities ($n_{\mathrm{e,u}} < 1.5 \cdot 10^{19}$ m^{-3}) in the blue dashed region of figure 5 the ion and electron temperatures of SOLPS-ITER diverge. These simulations are excluded in the comparison with DIV1D because it assumes equal ion and electron temperatures must likely implement flux limiters (see page 66 in [14]). Instead, we focus on high-density regimes in-line with the operating range of fusion reactors.

Figure 12 shows the target plasma density as function of upstream densities. The target density of DIV1D increases with the fourth power while SOLPS-ITER shows a linear trend. At high densities the DIV1D

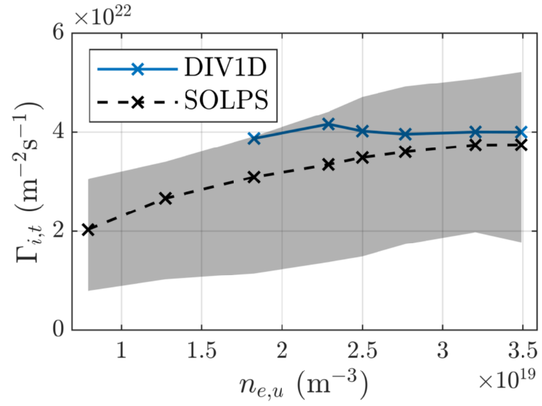

Figure 9. Comparison of the target ion flux (perpendicular to the target) for DIV1D and 1D mapped SOLPS-ITER simulations at various upstream electron densities. SOLPS-ITER and DIV1D do not display a target flux roll-over with increased upstream density.

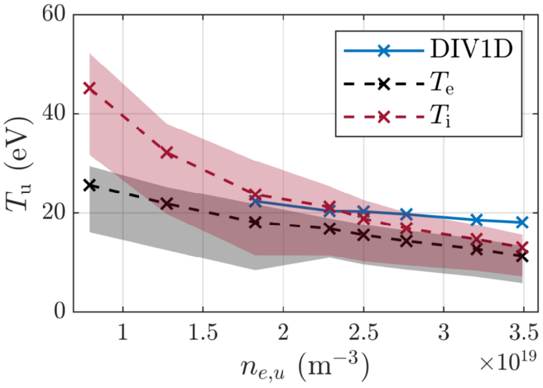

Figure 10. Comparison of the upstream temperature for DIV1D and 1D mapped SOLPS-ITER simulations at various upstream electron densities. The trend of DIV1D is weaker resulting in a five eV higher upstream temperature for the highest density compared to SOLPS-ITER.

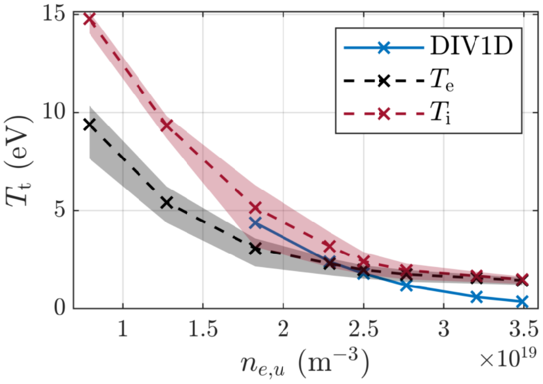

Figure 11. Comparison of the target temperature for DIV1D and 1D mapped SOLPS-ITER simulations at various upstream electron densities. At low densities the ion and electron temperature of SOLPS-ITER diverge. The target temperature of DIV1D drops a few eV below SOLPS-ITER for densities above $n_{\mathrm{e,u}} = 3 \cdot 10^{19}$ (m^{-3}).

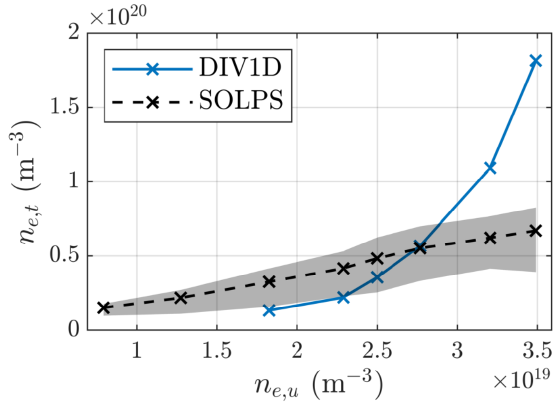

Figure 12. Comparison of the target density for DIV1D and 1D mapped SOLPS-ITER simulations at various upstream electron densities. The target density of DIV1D changes to the fourth power, contrasting to the linear trend of SOLPS-ITER.

target density is a factor two or three larger than that of SOLPS-ITER. The target ion flux scales with target density times the thermal velocity with the root of the temperature. Hence the fourth order evolution of the target density is connected to the target temperature that drops below SOLPS-ITER.

Finally, the momentum and power loss fractions are compared. The momentum and power loss fractions are calculated without volumetric integration for consistency between 1D mapped SOLPS-ITER and DIV1D using

$$f_{\mathrm{mom}}^{\mathrm{wovi}} = 1 - p_{\mathrm{tot,t}}/p_{\mathrm{tot,u}}, \tag{13}$$

and

$$f_{\mathrm{pwr}}^{\mathrm{wovi}} = 1 - \varepsilon_{\mathrm{f}} q_{\parallel,\mathrm{t}}/q_{\parallel,\mathrm{u}}, \tag{14}$$

with $p_{\mathrm{tot,u/t}}$ the total target and upstream pressure, ε_{f} the effective flux expansion (taken as $\varepsilon_{\mathrm{f}} = 2.3$ for presented power loss fractions) and $q_{\parallel,\mathrm{u}}$ the upstream heat flux [**?**]. The target heat flux is calculated as

$$q_{\parallel,\mathrm{t}} = T_{\mathrm{e,t}} \Gamma_{\parallel,\mathrm{t}} e \gamma, \tag{15}$$

where $T_{\mathrm{e,t}}$ is the target temperature, e the electron charge, γ the heat transmission factor, and $\Gamma_{\parallel,t}$ the target ion flux parallel to the field magnetic field [**?**]. The ion flux is directly obtained from simulation data.

The power and momentum loss fractions are depicted in figure 13. From low to high upstream densities, we observe a monotonic increase in momentum and power loss fractions for both DIV1D and SOLPS. The power losses of DIV1D are first lower than SOLPS-ITER and higher at high densities. Momentum losses are first similar and then overestimated by DIV1D. The discrepancy in power losses might again be a result of simplified carbon radiation functions [18, 19], but could also result from the omission of plasma molecule interactions causing additional hydrogenic energy losses [22].

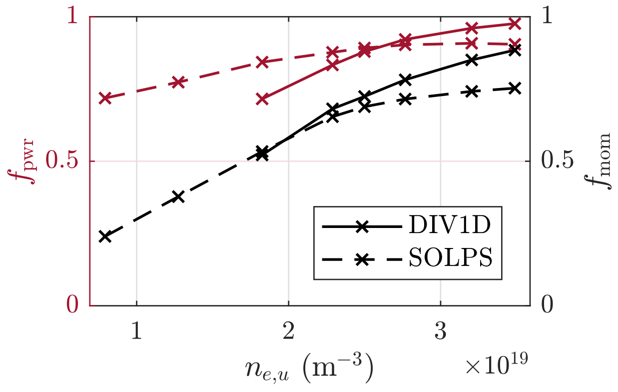

Figure 13. Comparison of power and momentum loss fractions for DIV1D and 1D mapped SOLPS-ITER simulations at various upstream electron densities.

The larger momentum losses in DIV1D could be attributed to the omission of momentum conservation for the neutral population, losing all momentum from the plasma in charge-exchange collisions [8,19]. An in-depth analysis of neutral descriptions in the scrape-off layer is available in [23] and would form the basis for further investigations.

To summarize, DIV1D was benchmarked on a set of SOLPS-ITER simulations to test if DIV1D can self-consistently describe the scrape-off layer plasma in the divertor. Reasonable agreement of profiles across a range of simulations was obtained and discrepancies were identified. The discrepancies are hypothesized to originate from descriptions in DIV1D of carbon radiation functions, the omission of molecules, and the omissions of neutral momentum and energy balances. These features were present in the SOLPS-ITER simulations. The following section focuses on the role of cross-field transport in DIV1D simulations for the agreement that was obtained with SOLPS-ITER.

5. The role of cross-field transport in 1D simulations of divertor detachment

Although considerable work has been devoted to reduced 1D models of the scrape-off layer [6–9, 18, 19], modeling research has tended to focus on qualitative results arguing that cross-field transport mainly influences quantitative results. A notable exception is [7], that included a correction for cross-field transport originating from 2D solutions and showed that a 1D model (SOLF1D) can quantitatively agree to 2D solutions. We took this one step further in the previous section and modeled cross-field transport in DIV1D through an effective flux expansion factor and an exchange time for neutrals in the divertor with a gas background, obtaining reasonable agreement to SOLPS-ITER. The following sections present simulations of DIV1D without flux expansion and without neutral gas background to highlight the role of cross-field transport in 1D simulations of the divertor.

5.1. *The role of cross-field plasma transport*

This section elaborates on the role of the flux expansion parameter ε_{f} in DIV1D to model cross-field transport that is observed in SOLPS-ITER solutions. To this end, the DIV1D simulations from the previous section are repeated with a flux expansion of $\varepsilon_{\mathrm{f}} = 1.1$, corresponding to the flux expansion in the magnetic equilibrium ($R_{\mathrm{t}}/R_{\mathrm{u}}$).

The profiles of DIV1D without transport based flux expansion are depicted in figure 14. It can be seen that the gradual decrease in heat flux density is now absent in the DIV1D results. As a result of the discrepancy in heat flux, the temperature profile is significantly higher across the leg and only decreases near the target. The increased temperature decreases upstream charge exchange and recombination rates and alters the particle balance. The altered particle balance results in a flow reversal with negative upstream velocities. The contrasting results in figures 14 and 6 show that it is both reasonable and necessary to model the effect of cross-field plasma transport with an effective flux expansion factor ε_{f}. This is one of the main conclusions of this work towards reduced 1D models of the scrape-off layer. As the total expansion factor ε_{f} depends on the width of the heat flux distribution along the leg, DIV1D still relies on predictions of the heat flux width [24,25].

5.2. *The role of cross-field neutral transport*

This section elaborates on the role of cross-field neutral transport in 1D simulations of the scrape-off layer. As neutrals experience no magnetic force, they move freely across magnetic fields such that transport is governed by collisions with particles. To account for neutral transport across flux tubes, transport coefficients are typically projected on the direction of the magnetic field (e.g. θ in equation 7) [6,8]. In addition, DIV1D contains the time-scale τ_{n} to account for neutrals that leave and enter the scrape-off layer along the leg.

In the following subsections we evaluate DIV1D simulations where neutrals are not exchanged between background gas and divertor inventories (i.e. $n_{\mathrm{b}} = 0$ m^{-3} and $\tau_{\mathrm{n}} = 1$ s). Instead a fraction of the target recycling flux is redistributed across the leg (i.e. $f_{\mathrm{r}} = 0.7$) in order to model the redistribution of recycling neutrals via the neutral volume outside the scrape-off layer. The redistributed fraction $f_{\mathrm{r}} = 0.7$ was chosen to obtain profiles of DIV1D that are similar to 1D mapped SOLPS-ITER profiles at an upstream density of $n_{\mathrm{e,u}} = 2.5 \cdot 10^{19}$ m^{-3}. As such f_{r} represents a considerable alternative method to model

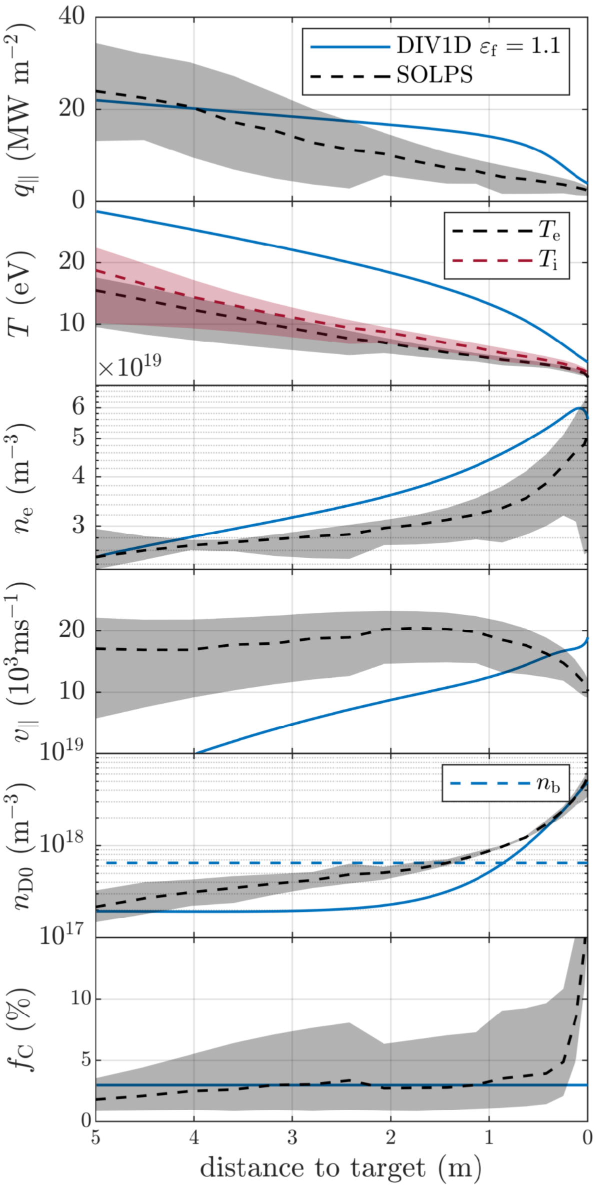

Figure 14. Comparison of DIV1D using $\varepsilon_f = 1.1$ with SOLPS simulation 150683 (second dashed black line in figure 5). The profiles of DIV1D for the heat flux, temperature and velocity do not correspond to 1D mapped SOLPS-ITER (in contrast to previous results with $\varepsilon_f = 2.3$ in figure 6).

the redistribution of neutrals along the leg via the volume outside the scrape-off layer.

5.2.1. Detachment development of DIV1D without neutral gas background compared to SOLPS-ITER

This subsection compares DIV1D with redistribution fraction $f_r = 0.7$) to 1D mapped SOLPS-ITER. The comparison focuses on the target ion flux, target temperature, and two-point loss fractions. The aim is to investigate the influence of the neutral gas background in solutions of DIV1D.

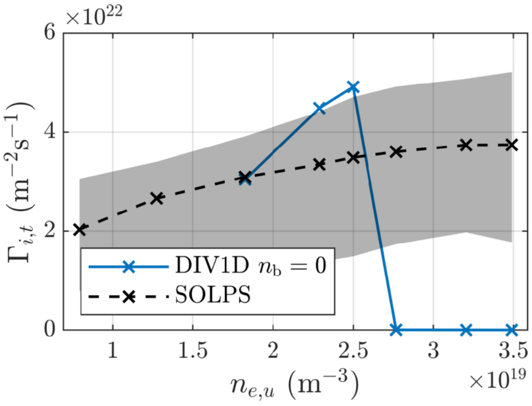

Figure 15. Comparison of the target ion flux (perpendicular to the target) for DIV1D without neutral gas background and 1D mapped SOLPS-ITER simulations at various upstream electron densities.

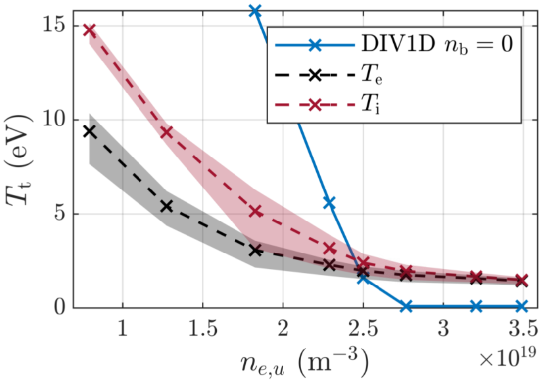

Figure 16. Comparison of the target temperature for DIV1D without neutral gas background and 1D mapped SOLPS-ITER simulations at various upstream electron densities.

Figure 15 depicts the target ion flux as function of upstream density for DIV1D with a redistribution fraction $f_r = 0.7$ together with values from 1D mapped SOLPS-ITER. It can be seen that the target ion flux of DIV1D suddenly drops to extremely low values.

The target temperatures are visible in figure 16. It can be seen that, compared to SOLPS-ITER, the target temperature of DIV1D without neutral gas background is more sensitive to the upstream density and decreases a factor three faster with upstream density. Consequently, target temperatures correspond for an upstream density of $2.5 \cdot 10^{19}$ m^{-3}, but not for both adjacent SOLPS-ITER simulations.

Momentum and power loss fractions are again calculated by means of equations 13 and 14 and can be seen in figure 17. Following the inverse of the target temperature, it can be seen that the momentum and power loss fractions increase a factor three faster than SOLPS-ITER and reach 100% at an upstream density of $2.8 \cdot 10^{19}$ m^{-3}.

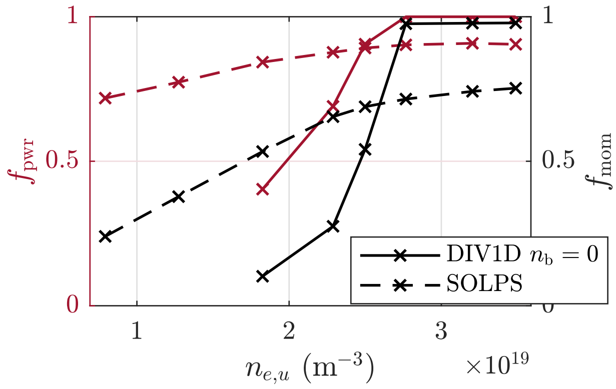

Figure 17. Comparison of power and momentum loss fractions for DIV1D and 1D mapped SOLPS-ITER simulations at various upstream electron densities. Without neutral gas background

The observations for target temperature, target flux and loss fractions of DIV1D simulations without neutral gas background (i.e. using $f_{\mathrm{r}} = 0.7$) show that solutions are more sensitive to the upstream density compared to DIV1D simulations with neutral gas background (e.g. figure 9). The following subsection evaluates a simulation of DIV1D with momentum and power loss fractions of 100% to investigate this sensitivity and understand why the solution of the target ion flux suddenly drops for increased upstream densities.

5.2.2. Comparing detached profiles of DIV1D without neutral gas background to 1D mapped SOLPS-ITER The profiles of DIV1D for a high upstream density of $n_{\mathrm{e,u}} = 3.2 \cdot 10^{19}$ m^{-3} are depicted in figure 18. Compared to the profiles of 1D mapped SOLPS-ITER, it is clear that DIV1D is in a different kind of solution. In DIV1D the target temperature is 0.1 eV (the minimum allowed value) and is part of an uniform low pressure and temperature region that extends a few meters from the target. Around a distance of 2.5 meters to the target the electron density abruptly rises two orders of magnitude reaching $3 \cdot 10^{20}$ m^{-3} to gradually fall below 10^{18} m^{-3} near the target. The neutral density is high in front of the target and decreases around 2.5 meters to the target due to ionization. The high value is a consequence of the neutral model which does not account for neutral losses perpendicular to flux surfaces thus confining all recycled neutrals inside the modeled flux tube. The energy losses for ionization correspond to a nonzero slope in the heat flux and a rise in temperature such that carbon radiation can become a large channel for energy losses around 7 eV. Above four meters to the target the temperature profile gradually increases as the heat flux and upstream density converge to the boundary conditions that follow from the 1D mapped SOLPS-ITER simulation. Since the temperature and ion flux at the target are reduced by over a factor 100 compared to upstream, losing all the power and particles, the DIV1D solution is clearly a fully ”detached” state. The question to answer is what causes DIV1D to transition into this detached regime and how does this relate to the sudden drop of target ion flux as was observed in figure 15.

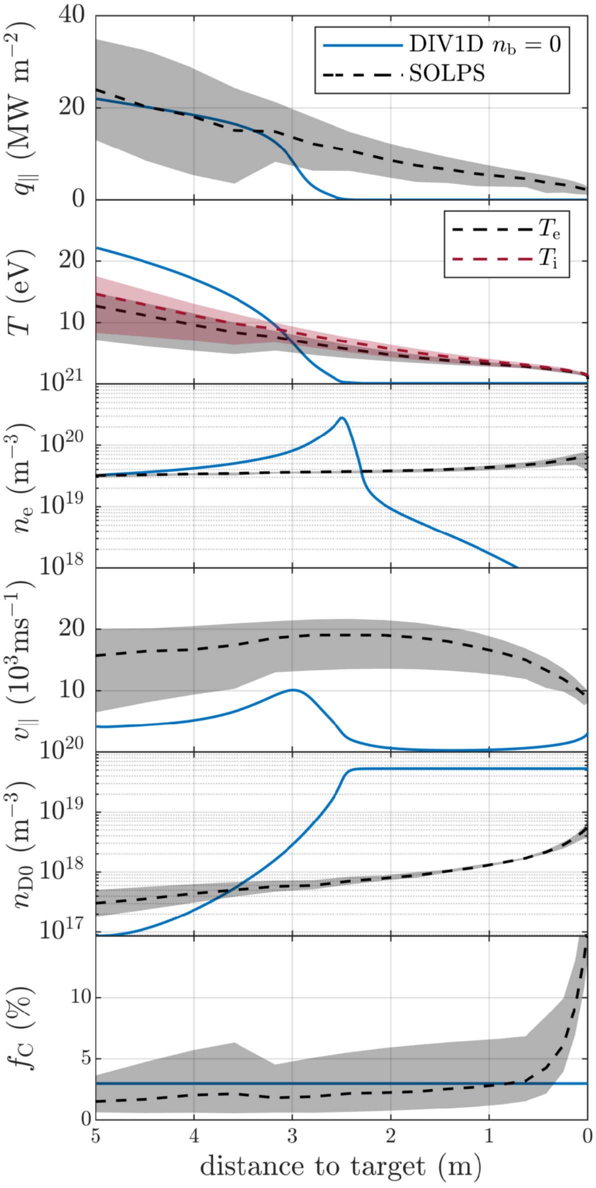

Figure 18. Comparison of DIV1D without neutral gas background to SOLPS-ITER simulation 150688 with $n_{\mathrm{e,u}} = 3.2 \cdot 10^{19}$(m^{-3}).

5.2.3. Ionization-recombination instability The sudden transition in DIV1D with $f_{\mathrm{r}} = 0.7$ seems related to the ionization-recombination instability as detailed in [18]; stating that the heat flux q into the region where the plasma recycles/recombines must exceed the ionization energy losses to the neutral flux $E_{\mathrm{ion}}\Gamma_{\mathrm{ion}}$ for a stationary solution as follows

$$q > E_{\text{ion}}\Gamma_{\text{ion}} \tag{16}$$

The ionizing flux $\Gamma_{\text{ion}} = f_{\text{ion}}\Gamma_{\text{neutral}}$ is governed by the neutrals that diffuse from the recombination region through a cold ”plasma buffer” into the upstream ionizing region Γ_{neutral} and the fraction of this flux that is ionized f_{ion}. As the neutral density increases near the target, the neutral flux that ionizes also increases and causes a violation of equation 16. As a result the target temperature drops and the plasma starts to recombine to equilibrate. Recombination causes a source of neutrals in the plasma itself which leads to a larger source of neutrals in the ionizing region upstream. This cools the upstream plasma and causes both the ionization and recombination region to shift upwards. The neutral gas background in DIV1D and the exchange of neutrals with this background gas reduce the neutral density in front of the target and increase the neutral density upstream. This reduces the neutral density gradient and flux into the ionization region and thereby the energy loss through ionization. The constrain in parallel neutral flux and thereby energy loss through ionization can prevent solutions from violating equation 16. Thus the exchange time and the neutral gas background are key parameters for the ionization-recombination instability to occur.

6. Conclusions and discussion

Fusion reactor power plants have to optimize both core and divertor performance. The core requires high densities, temperature and long confinement times to maximize fusion yields while the divertor requires low temperatures to protect the wall and good compression of impurities to pump/remove Helium. The trade-off between the divertor and core can be expressed in the location of impurity emission extinction fronts (e.g. for carbon [1]). Active control of such fronts is required to protect the wall, obtain efficient Helium pumping and circumvent instabilities originating from radiation close to the X point [1, 19, 26].

In this paper we presented DIV1D, a new 1D dynamic divertor model, that is being developed to guide heat exhaust control efforts for fusion reactors. The 2D equilibria of SOLPS-ITER were mapped to 1D by averaging over the full width at half the maximum of the heat flux distributions. Using this mapping, it was shown in section 4 that DIV1D reasonably agrees with SOLPS-ITER over a range of simulations and can transition between these solutions. Following section 5, these results are beyond doubt bound to the inclusion of effective flux expansion and the exchange of neutrals in the SOL with a gas background to model cross-field transport effects in DIV1D.

6.1. Cross-field transport

The mapping of SOLPS-ITER equilibria into 1D profiles along the leg was essential for the benchmark of DIV1D. Following studies on the width of the heat flux profile [3, 15, 24], we accepted that the heat flux does not flow in perfect magnetic flux tubes and averaged the FWHM of the heat flux distribution to map 2D SOLPS-ITER equilibria into 1D profiles. There are however cases for which the equilibria might not be captured in 1D, for instance when the resonant magnetic perturbations for Edge Localized Mode (ELM) suppression cause secondary peaks in the heat flux [27]. Therefore, efforts were made to add value intervals (shaded areas) that are sensitive for cases where features cannot be captured in 1D. This was apparent near the X-point where large value intervals motivated the selection of the upstream point around five meters from the target. In the first five meters in front of the target the match between DIV1D and mapped SOLPS-ITER solutions not only showed that DIV1D can describe the divertor plasma in 1D but also that the 1D interpretation of SOLPS-ITER is physical as it corresponds to the 1D representation of DIV1D. Our mapping of 2D equilibria to 1D profiles can be useful beyond benchmarks of 1D codes. For instance, to map 2D simulations and parameterize the momentum and energy loss fractions of the entire divertor with the two-point model format by Kotov and Reiter in [28]. Such a description remains valid under the influence of drift related heat flux migration.

The ability of DIV1D to match 1D mapped SOLPS-ITER simulations relies to a great extend on the effective flux expansion factor to account for cross-field plasma transport. As explained in [18], convective and cross-field transport can extend the region of radiative losses more than permitted in DIV1D as it only evaluates the Coronal Carbon equilibrium of Post et al. [29]. The discrepancy in temperature drop between DIV1D and SOLPS-ITER for high densities in figures 10 and 11 might therefore be resolved by extending the radiative loss region. Moreover, for cases with high impurity concentrations (e.g. when seeding nitrogen) the extension of the radiative loss region could be essential for DIV1D to match SOLPS-ITER and experimental results.

The exchange of neutrals in the SOL with a neutral gas background in DIV1D is a unique feature that is not present in previous reduced models reported in [6, 8, 9]. In those models the neutral gas background n_{b} was omitted such that the neutral residence time τ_{n} is a pure sink or source of particles. In DIV1D it is a source upstream and a sink near the target. The authors in [7] do consider a more complicated neutral particle source, but this is directly taken from (a legacy version of) the SOLPS-ITER code and not self-consistent. The neutral gas background was found to qualitatively change dynamics (i.e. the occurrence of the ionization-recombination instability) and is essential for quantitative agreement over a range of upstream densities (see section 5).

6.2. Future work

The comparison between SOLPS-ITER and DIV1D pointed to discrepancies that might be resolved in the future. To extend towards low density regimes, electron and ion temperatures could be computed separately and flux limiters could be introduced. To improve in medium densities, radiation losses could be adjusted for transport and molecules could be added. For better agreement in high densities, one could evaluate the role of molecules [22, 30] or neutral momentum and energy conservation. Especially momentum conservation is of interest as [8] showed that the upstream density for which the ion target flux rolls-over reduces significantly when neutral momentum is conserved.

Most importantly, the dynamics of DIV1D should be validated. In the exploration of designs, tests, and verification of controllers a multitude of dynamic models is required ranging in computation times from real-time, to minutes, days, and months. DIV1D might be useful as it computes 20 ms in a few minutes on a single core of an eight year old Xeon. At the basis, however, lies validation on control-relevant dynamics as identified in experiments.

Appendix A. Atomic Rates

In this work, the atomic rates from the AMJUEL data base are used. The rates from AMJUEL are also being used for the EIRENE neutral particle Monte Carlo code [31]. The following sections elaborate on the atomic rates used in DIV1D.

Appendix A.1. Charge Exchange

The default option uses the charge exchange rate as specified in section 2.19 reaction 3.1.8 of the AMJUEL data base for the total charge exchange rate of Hydrogen [31]. This uses a fit function of the form

$$\langle \sigma_{\mathrm{cx}} v \rangle = 10^{-6} \exp\left(\sum_{i=0}^{8} b_i (\ln T)^i\right) (\mathrm{m}^3/\mathrm{s}) \tag{A.1}$$

with the fitting constants b_i. Note that the factor 10^{-6} stems from the use of the units cm^3/s for the reaction rates in AMJUEL.

Charge exchange rates for the Hydrogen isotopes like Deuterium and Tritium are obtained by the same expressions given above, but using a rescaled temperature multiplied with the factor m_p/m_i, i.e. the ratio of the proton mass over the mass of the Deuterium or Tritium ion, respectively.

Appendix A.2. Ionization

The default option for calculation of the ionization rate is also obtained from the AMJUEL data base, which provides an effective ionization rate as calculated using a double fit function

$$\langle \sigma_{\mathrm{ion}} v \rangle = \\ 10^{-6} \exp\left(\sum_{i=0}^{8}\sum_{j=0}^{8} \alpha_{ij} (\ln \bar{n})^j (\ln T)^i\right) (\mathrm{m}^3/\mathrm{s}) \tag{A.2}$$

where the density is normalized as $\bar{n} \equiv n/10^{14}$ and the fitting coefficients α_{ij} are given in section 4.3 reaction 2.1.5 of the AMJUEL document for the case of the total ionization rate (including all excited states of the neutral hydrogen atoms).

Appendix A.3. Excitation and ionization energy losses

The sum of energy losses from ionization and excitation is obtained from the AMJUEL data base, which provides an effective excitation rate in terms of an averaged effective energy loss per ionization. This is calculated from a fit function of the same form as defined above for the ionization rate (A.2), i.e.

$$\langle E_{\mathrm{ion}} \sigma_{\mathrm{ion}} v \rangle + \langle E_{\mathrm{exc}} \sigma_{\mathrm{exc}} v \rangle = \\ 10^{-6} \exp\left(\sum_{i=0}^{8}\sum_{j=0}^{8} \alpha_{\mathrm{exc},ij} (\ln \bar{n})^j (\ln T)^i\right) (\mathrm{eVm}^3/\mathrm{s}) \tag{A.3}$$

with the coefficients $\alpha_{\mathrm{exc},ij}$ as tabulated in section 10.2 for reaction 2.5.1 of the AMJUEL document for the case of the total energy loss rate associated with Hydrogen ionization and excitation radiation.

Appendix A.4. Recombination

The recombination rate is used from the AMJUEL data providing the total effective recombination rate including 3 body recombination using again a fit function (A.2) as defined above for the ionization rate, now with the coefficients $\alpha_{\mathrm{rec},ij}$ as tabulated in section 4.6 reaction 2.1.8 of the AMJUEL document.

Also the energy lost and gained by the electrons due to radiative and three-body recombination is taken into account. The effective electron cooling rate from the associated processes is obtained from the fit specified in AMJUEL section 10.4 for the recombination reaction and taking into account the 13.6 eV potential energy gain per effective recombination event, i.e.

$$\langle E_{\mathrm{el}} \sigma_{\mathrm{rec}} v \rangle = \\ 10^{-6} \exp\left(\sum_{i=0}^{8}\sum_{j=0}^{8} \alpha_{\mathrm{rec,el},ij} (\ln \bar{n})^j (\ln T)^i\right) \tag{A.4} \\ -13.6 \langle \sigma_{\mathrm{rec}} v \rangle (\mathrm{eVm}^3/\mathrm{s})$$

where the effective recombination rate $\langle \sigma_{\mathrm{rec}} v \rangle$ is obtained from the fit specified before and the additional fit coefficients $\alpha_{\mathrm{rec,el},ij}$.

Appendix A.5. Impurity Radiation Losses

The impurity radiation losses are typically given in the form of a radiative cooling function $L_Z(T)$ where Z stands for the impurity species under consideration. For a given cooling rate function, the energy losses from impurity radiation are then given by

$$Q_{\mathrm{imp}} = -n^2 \xi_Z L_Z(T), \tag{A.5}$$

where ξ_Z is the concentration of the impurity. Post et al. [29] tabulated fit functions for the most relevant impurities in fusion plasmas using the general functional form of [29]

$$\log_{10} L_Z = \sum_{i=0}^{5} A(i)(\log_{10} T_{\mathrm{keV}})^i (\mathrm{cm}^3 \mathrm{erg/s}) \tag{A.6}$$

where T_{keV} is the temperature in keV. These functions do not take account of impurity transport effects that can shift and deform radiative cooling functions such that they peak at different temperatures and at slightly different rates. However, in the collisional regimes where the electron and ion temperatures are similar this effect can cause shifts of a few eV and reduce cooling rates by a few percent. Such details are currently out of scope for DIV1D as a control oriented model to study the dynamics of detachment.

Appendix B. DIV1D: Input and Output

This appendix provides a list of the inputs and outputs for DIV1D. The input is read from a file named `input.txt` that provides two FORTRAN namelists. One of these lists contains the numerical settings and one the physical parameter settings. The numerical parameters are listed in table B1. The physics parameters are listed in table B2. Dynamic inputs require additional `*.dat` files to run DIV1D.

The output is written in `div1doutput.txt`. Firstly, most inputs that were provided via `input.txt` and the `*.dat` files have been appended to `div1doutput.txt` and represent the actual values used by DIV1D for input verification. Secondly, the outputs in terms of states: `density`, `velocity`, `temperature`, `neutral`, fluxes: `Gamma_n`, `Gamma_mom`, `q_parallel`, `neutral_flux`, and sources: `Source_n`, `Source_v`, `Source_Q`, `Source_neutral` are written.

Appendix C. Settings for DIV1D based on mapped SOLPS-ITER simulations

This appendix details how inputs for DIV1D can be determined based on mapped SOLPS-ITER simulations. The procedure to map SOLPS-ITER solutions from 2D to 1D is described in section 3.2. The following list explains how inputs for DIV1D could be determined directly based on mapped 1D SOLPS profiles:

- L: the leg in DIV1D starts five grid cells below the X-point, at the black line in figure 4. Starting below the X-point avoids artifacts in the SOLPS profiles and reduces the artifact influence on the averaged profile. Once a grid cell is selected, the length equals the incremental distance of the cells along the magnetic field to the target.
- $n_{\mathrm{e,u}}$, $q_{\parallel,\mathrm{u}}$: the upstream density and parallel heat flux are taken at the black line of the red flux profile average tube in figure 4. These parameters are thus boundary conditions for DIV1D
- $\sin(\theta)$: the pitch angle is determined by dividing the vertical poloidal distance by the leg length as follows $\sin(\theta) = |z_{\mathrm{u}} - z_{\mathrm{t}}|/L$. Alternative the angle is obtained by an average of the fraction of total and poloidal magnetic field along the leg, resulting in $\sin(\theta) \approx 0.061$.
- ξ_{C}: the carbon concentration is ideally selected from the SOLPS profile in the region with the highest carbon radiation. The profiles in figure 4 show that in the region at which the temperature is around 10 eV is located at 3 meters to the target while the mean carbon concentration is approximately 2% away from the target and 10% near the target. To avoid the high target carbon concentrations, the median value of the flux profile averaged SOLPS profile is selected.
- n_{b}: the neutral gas background density is taken as the median value in the mapped averaged profile to reduce sensitivity to high target densities from recycling sources.
- $A_{\mathrm{t}}/A_{\mathrm{u}}$: the expansion of the area is calculated as follows. The area of grid cells in the poloidal plane are mapped to be perpendicular to the magnetic field by multiplying with $A_\perp = A_\theta \cos(\theta)$. As the heat flux migrates across flux surfaces the area of the cells that are covered are summed. The ratio between upstream and target area of the FHWM heat flux channel then represents the effective flux expansion factor as $A_{\mathrm{t}}/A_{\mathrm{u}} = \varepsilon_{\mathrm{f}}$.

Not all values in table C1 directly used as input for the benchmark simulations in section 4. For the benchmark simulations, the upstream density and neutral gas background density are explicitly varied. A single value was selected for other parameters to have a concise description and because they are relatively constant across 1D mapped SOLPS-ITER simulations.

Table B1. **Namelist `div1d_numerics` setting parameters controlling the numerical implementation.**

variable name	description
`Nx`	integer: number of points in the grid along the field line (default: 500)
`delta_t`	real: time step size (default: 1.0D-06)
`viscosity`	real: numerical viscosity (default = 5)
`abstol`	real: absolute value of tolerance in numerical integration (default: 1.0D-4)
`reltol`	real: relative value of tolerance in numerical integration (default: 1.0D-4)

Table B2. **Namelist `div1d_physics` setting parameters controlling the physics of the problem solved.**

variable name	description
`L`	real: length of the field line between upstream and target (default: 5.0D1 m)
`mass`	real: mass of the main plasma ion (default: 3.3436D-17 kg for D)
`gamma`	real: sheath heat transmission factor (default: 6D0)
`sintheta`	real: sinus of angle theta between B-field and target plate (default: 0.1D0)
`q_par`	real: upstream parallel heat flux (default: 1.0D8 $\mathrm{Wm^{-2}}$)
`flux_expansion`	real: expansion of total flux from X-point to target (default: 1.0D0)
`upstream_n`	real: upstream plasma density (default: 1.0D20 $\mathrm{m^{-3}}$)
`neutral_background`	real: homogeneous neutral gas background density (default: 0.0D0 $\mathrm{m^{-3}}$)
`carbon_concentration`	real: concentration of Carbon impurity ions (default: 1.0D-2)
`recycling`	real: fraction of ion flux on target recycled as neutral (default: 1.0D0)
`redistributed_fraction`	real: distributed fraction of recycling neutral along the leg (default: 0.0D0)
`neutral_residence_time`	real: time scale in which neutral are lost from the SOL (default: 1.0D20 s)
`gas_puff_source`	real: total particle source from gass puff along flux tube (default: 0.0D0 $\mathrm{m^{-2}}$)

Table C1. Inputs for DIV1D that follow from mapped SOLPS profiles.

SOLPS Simulation	$n_\mathrm{e,u}$ 10^{19} ($\mathrm{m^{-3}}$)	n_b 10^{17} ($\mathrm{m^{-3}}$)	L (m)	$q_{\parallel,\mathrm{u}}$ ($\mathrm{MWm^{-2}}$)	ξ_C (a.u.)	$\sin(\theta)$ (a.u.)	$A_\mathrm{t}/A_\mathrm{u}$ (a.u.)
150678	1.83	3.63	5.04	22.38	0.038	0.058	2.2
150681	2.29	5.06	5.02	20.29	0.036	0.059	2.3
150683	2.50	6.49	5.01	23.50	0.030	0.059	2.5
150685	2.77	8.09	5.01	23.82	0.026	0.059	2.7
150688	3.20	10.34	5.00	23.47	0.025	0.059	2.7
150691	3.49	12.49	4.99	20.69	0.026	0.059	2.4

Appendix D. Two point code verification

The DIV1D code has been checked for code errors following [16] by integrating the energy balance in equation 4 as follows

$$\begin{aligned}
&\int_t^u \frac{\partial}{\partial x}\left(\frac{q_\parallel}{B}\right)dx = \int_t^u \frac{v_\parallel}{B}\frac{\partial p}{\partial x}dx + \int_t^u \frac{S_\mathrm{ene}}{B}dx,\\
&\underbrace{\left(1-\frac{q_{\parallel,\mathrm{t}}}{q_{\parallel,\mathrm{u}}}\frac{B_\mathrm{u}}{B_\mathrm{t}}\right)}_{f_\mathrm{pwr}^\mathrm{wovi}} = \underbrace{\int_\mathrm{t}^\mathrm{u}\left[\frac{v_\parallel}{B}\frac{\partial p}{\partial x}+\frac{S_\mathrm{ene}}{B}\right]dx\frac{B_u}{q_{\parallel,\mathrm{u}}}}_{f_\mathrm{pwr}^\mathrm{wivi}},
\end{aligned} \tag{D.1}$$

where the left term represents the power loss fraction based on target and upstream outputs of the code without evaluating volume integrals (wivi) as presented in equation 14. The right term represent the power loss fraction that can be calculated from the detailed profiles and source terms of DIV1D. For the momentum balance in equation 3 the dynamic term is expanded as follows

$$\frac{\partial}{\partial x}\frac{nmv_\parallel^2}{B} = \frac{1}{B}\frac{\partial}{\partial x}nmv_\parallel^2 - \frac{1}{B^2}nmv_\parallel^2\frac{\partial B}{\partial x}, \tag{D.2}$$

such that the momentum balance can be readily integrated over the leg

$$\left[\frac{\partial}{\partial x}\left(nmv_\parallel^2 + p\right)\right]_\mathrm{t}^\mathrm{u} = \int_\mathrm{t}^\mathrm{u} \left(\frac{1}{B} nmv_\parallel^2 \frac{\partial B}{\partial x} + S_\mathrm{mom}\right) dx,$$

$$\underbrace{1 - \frac{p_\mathrm{tot,t}}{p_\mathrm{tot,u}}}_{f_\mathrm{mom}^\mathrm{wovi}} = \underbrace{\int_t^u \left(\frac{1}{B} nmv_\parallel^2 \frac{\partial B}{\partial x} + S_\mathrm{mom}\right) dx/p_\mathrm{tot,u}}_{f_\mathrm{mom}^\mathrm{wivi}}, \tag{D.3}$$

Again the left hand side represents the momentum loss fraction without evaluating volume integrals (wovi, see also equation 13) and the right hand side with detailed integrals (wivi). The left and right hand sides of equations D.1 and D.3 were evaluated using the code output of DIV1D and results are presented in table D1 and D2 for the simulations in this paper.

Acknowledgments

This work has been carried out within the framework of the EUROfusion Consortium, funded by the European Union via the Euratom Research and Training Programme (Grant Agreement No. 101052200 — EUROfusion). Views and opinions expressed are however those of the author(s) only and do not necessarily reflect those of the European Union or the European Commission. Neither the European Union nor the European Commission can be held responsible for them.

References

[1] T. Ravensbergen, M. van Berkel, A. Perek, C. Galperti, B. P. Duval, O. Février, R. J. van Kampen, F. Felici, J. T. Lammers, C. Theiler, J. Schoukens, B. Linehan, M. Komm, S. Henderson, D. Brida, and M. R. de Baar, "Real-time feedback control of the impurity emission front in tokamak divertor plasmas," *Nat. Commun.*, vol. 12, no. 1, pp. 1–9, 2021.

[2] E. Westerhof, H. J. de Blank, R. Chandra, and J. P. Frankemölle, "A 1D code for studies of divertor detachment dynamics," *47th EPS Conf. Plasma Physics, EPS 2021*, vol. 2021-June, pp. 1048–1051, 2021.

[3] M. Komm, I. Khodunov, J. Cavalier, P. Vondracek, S. Henderson, J. Seidl, J. Horacek, D. Naydenkova, J. Adamek, P. Bilkova, P. Bohm, A. Devitre, M. Dimitrova, S. Elmore, M. Faitsch, P. Hacek, J. Havlicek, A. Havranek, M. Imrisek, J. Krbec, M. Peterka, R. Panek, O. Samoylov, M. Sos, M. Tomes, K. Tomova, and V. Weinzettl, "Divertor impurity seeding experiments at the COMPASS tokamak," *Nucl. Fusion*, vol. 59, no. 10, 2019.

[4] M. Van Berkel, A. De Cock, T. Ravensbergen, G. M. Hogeweij, H. J. Zwart, and G. Vandersteen, "A systematic approach to optimize excitations for perturbative transport experiments," *Phys. Plasmas*, vol. 25, no. 8, pp. 1–14, 2018.

[5] J. Koenders, M. Wensing, T. Ravensbergen, O. Février, A. Perek, M. van Berkel, the TCV Team, and the EUROfusion MST1 Team, "Systematic extraction of a control-oriented model from perturbative experiments and SOLPS-ITER for emission front control in TCV," *Nucl. Fusion*, vol. 62, no. 6, p. 066025, 2022.

[6] S. Nakazawa, N. Nakajima, M. Okamoto, and N. Ohyabu, "One-dimensional simulation on stability of detached plasma in a tokamak divertor," *Plasma Phys. Control. Fusion*, vol. 42, no. 4, pp. 401–413, 2000.

[7] E. Havlíčková, W. Fundamenski, F. Subba, D. Coster, M. Wischmeier, and G. Fishpool, "Benchmarking of a 1D scrape-off layer code SOLF1D with SOLPS and its use in modelling long-legged divertors," *Plasma Phys. Control. Fusion*, vol. 55, no. 6, 2013.

[8] B. D. Dudson, J. Allen, T. Body, B. Chapman, C. Lau, L. Townley, D. Moulton, J. Harrison, and B. Lipschultz, "The role of particle, energy and momentum losses in 1D simulations of divertor detachment," *Plasma Phys. Control. Fusion*, vol. 61, no. 6, 2019.

[9] S. TOGO, M. NAKAMURA, Y. OGAWA, K. SHIMIZU, T. TAKIZUKA, and K. HOSHINO, "Effects of Neutral Particles on the Stability of the Detachment Fronts in Divertor Plasmas," *Plasma Fusion Res.*, vol. 8, no. 0, pp. 2403096–2403096, 2013.

[10] P. C. Stangeby, "The Plasma Boundary of Magnetic Fusion Devices," *Plasma Bound. Magn. Fusion Devices*, 2000.

[11] M. Wensing, B. P. Duval, O. Février, A. Fil, D. Galassi, E. Havlickova, A. Perek, H. Reimerdes, C. Theiler, K. Verhaegh, and M. Wischmeier, "SOLPS-ITER simulations of the TCV divertor upgrade," *Plasma Phys. Control. Fusion*, vol. 61, no. 8, 2019.

[12] S. Wiesen, D. Reiter, V. Kotov, M. Baelmans, W. Dekeyser, A. S. Kukushkin, S. W. Lisgo, R. A. Pitts, V. Rozhansky, G. Saibene, I. Veselova, and S. Voskoboynikov, "The new SOLPS-ITER code package," *J. Nucl. Mater.*, vol. 463, pp. 480–484, 2015.

[13] M. Wensing, H. Reimerdes, O. Février, C. Colandrea, L. Martinelli, K. Verhaegh, F. Bagnato, P. Blanchard, B. Vincent, A. Perek, S. Gorno, H. De Oliveira, C. Theiler, B. P. Duval, C. K. Tsui, M. Baquero-Ruiz, and M. Wischmeier, "SOLPS-ITER validation with TCV L-mode discharges," *Phys. Plasmas*, vol. 28, no. 8, 2021.

[14] M. Wensing, "Drift-related transport and plasma-neutral interaction in the TCV divertor," *Ph.D. Thesis*, 2021.

[15] M. A. Makowski, D. Elder, T. K. Gray, B. Labombard, C. J. Lasnier, A. W. Leonard, R. Maingi, T. H. Osborne, P. C. Stangeby, J. L. Terry, and J. Watkins, "Analysis of a multi-machine database on divertor heat fluxes," *Phys. Plasmas*, vol. 19, no. 5, 2012.

[16] P. C. Stangeby, "Basic physical processes and reduced models for plasma detachment," *Plasma Phys. Control. Fusion*, vol. 60, no. 4, p. 44022, 2018.

[17] C. K.-W. Tsui, J. A. Boedo, O. Février, H. Reimerdes, C. Colandrea, and S. Gorno, "Relevance of ExB drifts for particle and heat transport in divertors," *Plasma Phys. Control. Fusion*, vol. 64, p. 065008, jun 2022.

[18] S. I. Krasheninnikov, M. Rensink, T. D. Rognlien, A. S. Kukushkin, J. A. Goetz, B. LaBombard, B. Lipschultz, J. L. Terry, and M. Umansky, "Stability of the detachment front in a tokamak divertor," *J. Nucl. Mater.*, vol. 266, pp. 251–257, 1999.

[19] B. Lipschultz, F. I. Parra, and I. H. Hutchinson, "Sensitivity of detachment extent to magnetic configuration and external parameters," *Nucl. Fusion*, vol. 56, no. 5, 2016.

[20] K. Verhaegh, B. Lipschultz, J. R. Harrison, B. P. Duval, A. Fil, M. Wensing, C. Bowman, D. S. Gahle, A. Kukushkin, D. Moulton, A. Perek, A. Pshenov, F. Federici, O. Février, O. Myatra, A. Smolders, and C. Theiler, "The role of plasma-molecule interactions on power and particle balance during detachment on the TCV tokamak," *Nucl. Fusion*, vol. 61, no. 10, 2021.

[21] K. Verhaegh, B. Lipschultz, J. Harrison, B. Duval, C. Bowman, A. Fil, D. S. Gahle, D. Moulton, O. Myatra, A. Perek, C. Theiler, and M. Wensing, "A study of the influence of plasma–molecule interactions on particle

Table D1. The power balance checks for the fraction $f^{\mathrm{wovi}}_{\mathrm{pwr}}/f^{\mathrm{wivi}}_{\mathrm{pwr}}$ calculated from equation D.1. The simulations with redistribution fraction $f_{\mathrm{r}} = 0.7$ have some code errors in the power balance.

SOLPS-ITER simulation	150678	150681	150683	150685	150688	150691
DIV1D base scan	0.9976	0.9975	0.9971	0.9967	0.9943	0.9923
DIV1D scan with $\varepsilon_{\mathrm{f}} = 1.1$	1.0054	1.0028	1.0000	0.9990	0.9973	0.9973
DIV1D scan with $f_{\mathrm{r}} = 0.7$	0.4789	0.8396	0.9605	1.0000	1.0000	1.0000

Table D2. The momentum balance checks for the fraction $f^{\mathrm{wovi}}_{\mathrm{mom}}/f^{\mathrm{wivi}}_{\mathrm{mom}}$ calculated from equation D.3. The errors on the momentum balance do not exceed 5%.

SOLPS-ITER simulation	150678	150681	150683	150685	150688	150691
DIV1D base scan	1.0019	1.0041	1.0032	1.0009	0.9938	0.9770
DIV1D scan with $\varepsilon_{\mathrm{f}} = 1.1$	0.9563	0.9698	0.9895	0.9940	0.9902	0.9914
DIV1D scan with $f_{\mathrm{R}} = 0.7$	0.9892	0.9973	0.9992	1.0000	1.0000	1.0000

balance during detachment," *Nucl. Mater. Energy*, vol. 26, 2021.

[22] K. Verhaegh, B. Lipschultz, B. P. Duval, O. Février, A. Fil, C. Theiler, M. Wensing, C. Bowman, D. S. Gahle, J. R. Harrison, B. Labit, C. Marini, R. Maurizio, H. De Oliveira, H. Reimerdes, U. Sheikh, C. K. Tsui, N. Vianello, and W. A. Vijvers, "An improved understanding of the roles of atomic processes and power balance in divertor target ion current loss during detachment," *Nucl. Fusion*, vol. 59, no. 12, 2019.

[23] D. A. Russell, J. R. Myra, and D. P. Stotler, "A reduced model of neutral-plasma interactions in the edge and scrape-off-layer: Verification comparisons with kinetic Monte Carlo simulations," *Phys. Plasmas*, vol. 26, no. 2, 2019.

[24] T. Eich, A. W. Leonard, R. A. Pitts, W. Fundamenski, R. J. Goldston, T. K. Gray, A. Herrmann, A. Kirk, A. Kallenbach, O. Kardaun, A. S. Kukushkin, B. Labombard, R. Maingi, M. A. Makowski, A. Scarabosio, B. Sieglin, J. Terry, and A. Thornton, "Scaling of the tokamak near the scrape-off layer H-mode power width and implications for ITER," *Nucl. Fusion*, vol. 53, no. 9, 2013.

[25] M. Chang, C. Sang, Z. Sun, W. Hu, and D. Wang, "The effects of particle recycling on the divertor plasma: A particle-in-cell with Monte Carlo collision simulation," *Phys. Plasmas*, vol. 25, no. 5, 2018.

[26] U. Stroth, M. Bernert, D. Brida, M. Cavedon, R. Dux, E. Huett, T. Lunt, O. Pan, and M. Wischmeier, "Model for access and stability of the X-point radiator and the threshold for marfes in tokamak plasmas," *Nucl. Fusion*, 2022.

[27] H. Frerichs, X. Bonnin, Y. Feng, L. Li, Y. Q. Liu, A. Loarte, R. A. Pitts, D. Reiter, and O. Schmitz, "Divertor detachment in the pre-fusion power operation phase in ITER during application of resonant magnetic perturbations," *Nucl. Fusion*, vol. 61, no. 12, 2021.

[28] V. Kotov and D. Reiter, "Two-point analysis of the numerical modelling of detached divertor plasmas," *Plasma Phys. Control. Fusion*, vol. 51, no. 11, 2009.

[29] D. E. Post, R. V. Jensen, C. B. Tarter, W. H. Grasberger, and W. A. Lokke, "Steady-state radiative cooling rates for low-density, high-temperature plasmas," *At. Data Nucl. Data Tables*, vol. 20, no. 5, pp. 397–439, 1977.

[30] K. Verhaegh, B. Lipschultz, B. P. Duval, A. Fil, M. Wensing, C. Bowman, and D. S. Gahle, "Novel inferences of ionisation and recombination for particle/power balance during detached discharges using deuterium Balmer line spectroscopy," *Plasma Phys. Control. Fusion*, vol. 61, no. 12, 2019.

[31] D. Reiter, "The EIRENE Code User Manual," *Inst. für Energ.*, p. 304, 2019.